

See discussions, stats, and author profiles for this publication at: <https://www.researchgate.net/publication/229046806>

Mott–Schottky and Charge–Transport Analysis of Nanoporous Titanium Dioxide Films in Air

ARTICLE *in* THE JOURNAL OF PHYSICAL CHEMISTRY C · MARCH 2007

Impact Factor: 4.77 · DOI: 10.1021/jp068354l

CITATIONS

37

READS

63

4 AUTHORS, INCLUDING:



Marius Nanu

thin film factory

35 PUBLICATIONS 799 CITATIONS

SEE PROFILE



Joop Schoonman

Delft University of Technology

605 PUBLICATIONS 8,929 CITATIONS

SEE PROFILE

Mott–Schottky and Charge-Transport Analysis of Nanoporous Titanium Dioxide Films in Air

Ryan O’Hayre,^{*,†} Marian Nanu,[‡] Joop Schoonman,[‡] and Albert Goossens[‡]

Department of Metallurgical and Materials Engineering, Colorado School of Mines, 1500 Illinois Street, Golden, Colorado 80401, and Delft Institute for Sustainable Energy, Delft University of Technology, 2628 BL Delft, The Netherlands

Received: December 5, 2006; In Final Form: January 26, 2007

We investigate the electrical properties of air-filled nanoporous TiO₂ films through Mott–Schottky (MS) and current–voltage (IV) analyses. Films of varying thickness and varying TiO₂ particle size are examined. Dark IV analysis indicates formation of an asymmetric Schottky-barrier junction between the nanoporous TiO₂ film and a graphite back contact. Upon increasing the film thickness and decreasing the particle size, diode rectification deteriorates while series resistance increases; these phenomena are attributed to resistive hopping charge transport between TiO₂ particles. Dramatic differences in the dark-IV extrapolated resistance of comparable thickness 300 and 9 nm films indicate that the transport physics may be substantially different between these two types of films in the dark. An effective medium model is developed that appropriately describes the dark MS data, indicating that the TiO₂ film behaves as a pure dielectric in the depletion region and that the internal surface area of the film does not contribute to the capacitance. Upon UV illumination, photodoping increases the TiO₂ film conductivity. Fermi-level splitting results in an ohmic graphite contact and current flow is generally limited by carrier transport rather than charge transfer to the contact. IV analysis based on a space charge limited current model provides mobility estimates of $\sim 1.7\text{--}3.4 \times 10^{-4} \text{ cm}^2 \text{ V}^{-1} \text{ s}^{-1}$ for the 9 nm diameter TiO₂ particle films and $\sim 1.8\text{--}3.5 \times 10^{-4} \text{ cm}^2 \text{ V}^{-1} \text{ s}^{-1}$ for 300 nm diameter TiO₂ particle films under AM 1.5 illumination. The close agreement between the illuminated-IV extrapolated electron mobility for both the 9 and 300 nm diameter TiO₂ particles suggests that the transport physics are likely similar in both films when illuminated.

I. Introduction

The low cost, ease of fabrication, wide availability, and high stability of porous nanocrystalline TiO₂ has led to its increasing deployment in a variety of functional applications. For example, it is extensively used in dye-sensitized solar cells (DSSCs),^{1,2} photocatalysis and photoelectrochemistry,^{3,4} electrochromics,⁵ and sensors.^{6,7} Despite its widespread application, the electrical properties of porous nanocrystalline TiO₂ are still poorly understood. Characterization and interpretation is complicated by structural disorder, high surface area, and the influence of defects.^{8,9} So far, most studies have focused on the properties of nanoporous TiO₂ films when immersed in an electrolyte, since this reflects the situation experienced in DSSCs and in most other applications.^{10–19} A general consensus has emerged from these TiO₂/electrolyte studies, yielding the following conclusions: (1) Surface states at the TiO₂/electrolyte interface strongly influence the electrical behavior of the system, affecting both charge-transport and recombination processes. (2) Mobile ionic species in the liquid electrolyte effectively screen the TiO₂ from any macroscopic electric fields, leading to the dominance of diffusion-based transport of electrons within the nanoporous TiO₂ film. (3) The low intrinsic conductivity of the TiO₂ film in combination with field screening means that under depletion conditions the potential drop across the nanoporous TiO₂ film should be sharply localized to the substrate/TiO₂ interface. These

conclusions have important ramifications for catalytic and photovoltaic applications of nanocrystalline TiO₂/electrolyte systems.

Despite the extensive research on TiO₂/electrolyte systems, however, far fewer studies have characterized the properties of porous nanocrystalline TiO₂ films in ambient air.^{8,20–22} Such research is needed, because air-based measurements are more likely to reflect the conditions presented by nonelectrolyte applications of nanoporous TiO₂ (like some sensor applications,²³ or the recently developed 3D nanocomposite inorganic solar cell^{24,25}). It should be expected that the electrical behavior of nanoporous TiO₂ will change significantly in the absence of an electrolyte, due to the loss of ion screening and changes in interfacial chemistry. For example, in air and vacuum based studies of nanoporous TiO₂, Nelson et al. observed significant changes in the electron transport and recombination behavior when varying the environmental conditions.^{8,20} They attributed these effects primarily to electron scavenging by surface absorbed species. In a separate study, Konenkamp observed reduced electron mobility in air-filled nanoporous TiO₂ films compared to electrolyte filled films.²² He hypothesized that charge transfer or surface passivation at the TiO₂/electrolyte interface may decrease the available trap states in electrolyte filled films compared to the air-filled case.

In this paper, the electrical properties of air-filled nanoporous TiO₂ films are further defined through Mott–Schottky (MS) and current–voltage (IV) analyses in dark and IV analysis under illumination. Films of varying thickness and varying TiO₂

* Address correspondence to this author. E-mail: rohayre@mines.edu.

[†] Colorado School of Mines.

[‡] Delft University of Technology.

TABLE 1: Characteristics of Samples Used in the Study

sample	crystallite size (nm)	nanoporous layer thickness (nm)
DL only	N/A	N/A
300nc-50nm	300	50
300nc-130nm	300	130
300nc-350nm	300	350
300nc-1100nm	300	1100
9nc-350nm	9	350
9nc-850nm	9	850
9nc-1150nm	9	1150

particle size are investigated. MS analysis as a function of film thickness is used to elucidate the distribution of the electric field in air-filled nanoporous TiO_2 films, while IV analysis provides insight into the charge-transport mechanisms and electron mobility.

II. Experimental Section

Nanoporous TiO_2 film structures in the configuration glass/TCO/ TiO_2 /graphite were prepared as follows. To eliminate the possibility of shorting, a thin (~ 200 nm) dense underlayer of anatase TiO_2 was first deposited onto transparent conductive oxide (TCO) coated glass substrates via the spray pyrolysis technique (described in detail in ref 25). Nanoporous TiO_2 film coatings were subsequently deposited via the doctor blade technique from commercially available precursor pastes (Solaronix, Inc.). Two different film types containing 9 and 300 nm TiO_2 nanocrystallites, respectively, were prepared. These will be referred to as 9nc and 300nc film types throughout this paper. By varying the viscosity of the precursor pastes via dilution with ethanol, films of varying thickness were produced ($0.05\text{--}1.15\text{ }\mu\text{m}$). Table 1 provides a summary of the samples used in this study. Sample 9nc-350nm in Table 1, for example, was a 350 nm thick film prepared from 9 nm diameter TiO_2 nanocrystallites. The “DL only” sample consisted of only the spray-coated dense TiO_2 layer without an overlying nanoporous film.

After annealing at $450\text{ }^\circ\text{C}$ for 6 h in air to remove organics, circular graphite electrodes (19.6 mm^2 in area) were applied to the top surfaces of the films. The graphite electrodes were painted onto the samples with conductive graphite ink. Electrode size was defined with use of a stencil mask. The graphite ink contained graphite flakes of approximately $30\text{ }\mu\text{m}$ diameter. In all electrical measurements, the top graphite electrode served as the working electrode, while the bottom TCO film served as the counter/reference electrode. Thus in forward bias, the graphite film was positive relative to the TCO electrode. Electron microscope cross-sectional images showed that graphite penetration into the nanoporous TiO_2 film was not a problem due to the large grain size ($\sim 30\text{ }\mu\text{m}$) of the graphite. Therefore, to a reasonable approximation, the contact geometry could be considered planar. For all samples, film thickness was quantified with a Detak 6M profilometer (Veeco Instruments). Porosity, determined by measuring the weight and film dimensions of witness samples, was estimated to be 56% ($\pm 5\%$) for the 9nc films and 66% ($\pm 3\%$) for the 300nc films. In both cases, within experimental error, porosity was independent of film thickness. For the thinnest (50 and 130 nm) film samples employing the 300 nm crystallites, porosity was not a meaningful descriptor since these films provided only partial surface coverage.

IV measurements were performed in the dark and in the light with a Princeton Applied Research 273 potentiostat/galvanostat. For measurements in the light, illumination was provided with

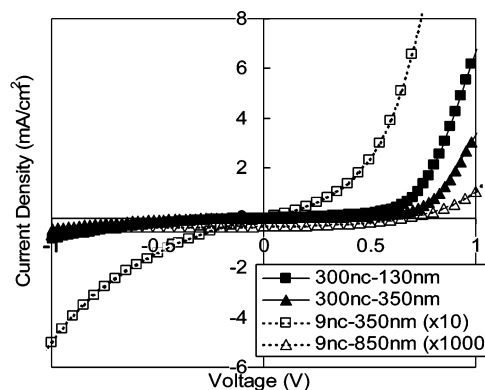
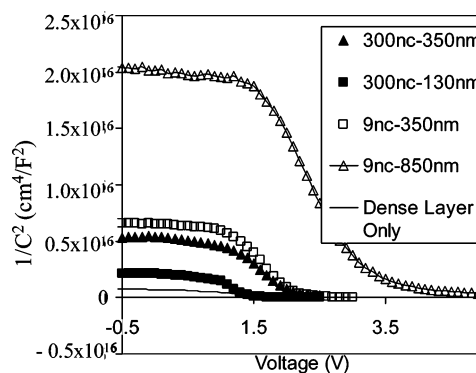
**a)****b)**

Figure 1. Dark IV curves (a) and corresponding dark MS curves (b) for selected 9nc and 300nc samples. The current–density values for the 9nc-350nm and 9nc-850nm IV curves have been amplified by a factor of 10 and 1000, respectively, for clarity.

a calibrated AM 1.5 solar simulator (Solar Constant 1200, K.H. Steuernagel Lichttechnik GmbH). MS measurements were acquired with a Solartron 1255 FRA in combination with a Princeton Applied Research 283 potentiostat/galvanostat. In all cases, a 10 mV sinusoidal excitation signal was employed to interrogate the capacitance. Capacitance was determined from single-frequency measurements at high frequency by assuming a simple series RC circuit model for the system. Capacitances calculated by using this approach were similar to capacitances extracted from full impedance spectrum fits (measured in the range $1\text{ MHz--}1\text{ Hz}$). Furthermore, the capacitances calculated from single-frequency measurements did not significantly vary in the range $1\text{ MHz--}10\text{ kHz}$. All data presented in this paper are from 100 kHz measurements. Area normalized capacitance values (units of F/cm^2) are employed in all equations and data results throughout. All measurements were made at room temperature and ambient humidity ($T = 20\text{ }^\circ\text{C}$, $\text{RH} \approx 60\%$).

III. Results and Discussion

A. Dark IV Analysis. Figure 1a presents typical dark IV responses for a series of 9nc and 300nc TiO_2 films of varying thickness. In all cases, an asymmetric, Schottky-barrier response is observed. Mott–Schottky measurements (presented in the next section) suggest that the rectifying junction occurs between the nanoporous TiO_2 film and the graphite back contact. We believe that the front contact (between F-doped SnO_2 and the spray deposited TiO_2 film) is ohmic, although recent reports suggest

TABLE 2: Dark IV Characteristics of the Investigated Samples

sample	G (mS/cm ²)	R (Ω cm ²)	n	J_0 (mA/cm ²)
DL only	0.385	19.2	3.2	1.1×10^{-3}
300nc-50nm	0.06	14.4	2.7	3×10^{-5}
300nc-130nm	0.17	21.3	3.1	1×10^{-4}
300nc-350nm	0.06	14.9	2.6	2.0×10^{-5}
300nc-1100nm	0.47	53.5	12	4×10^{-2}
9nc-350nm	0.2	532	4.2	9.5×10^{-3}
9nc-850nm	0.001	2860	8.1	5×10^{-6}

that this junction can also induce a Schottky-barrier response.²⁶ Our assignment of the rectifying junction to the graphite contact is bolstered by the fact that symmetric test cells of the configuration TCO/TiO₂/TCO show ohmic behavior while symmetric test cells of the configuration graphite/TiO₂/graphite show diode behavior.

The IV curves presented in Figure 1a can be analyzed by using a modified Schottky barrier diode-equation approach. In this approach, we assume that the current is limited by thermionic emission over the Schottky barrier, while neglecting tunneling or diffusion modifications. This assumption is reasonable over the voltage range (± 1 V) presented in Figure 1. While tunneling and diffusion are not considered, we find it necessary to take into account series resistance (R) and shunt (G) conductance losses, using a modified diode approach as described in ref 27:

$$J = J_0 \exp\left[\frac{e}{nkT}(V - RJ) - 1\right] + GV - J_{sc} \quad (1)$$

In this equation, n is the diode ideality factor, e is the electron charge, k is Boltzmann's constant, T is temperature, and J_0 is the exchange current. This equation assumes that the shunt conductance (G) is in parallel with the series combination of the diode plus the series resistance (R). Thus, G experiences the full voltage drop V , and the current flowing through the shunt conductance is given by $G \cdot V$ (rather than $G \cdot [V - RJ]$). We feel that this model adequately reflects the physical situation in our samples, since the shunt-conduction pathway likely corresponds to pinholes/shorts in our films that short both the TiO₂ layer and the diode interface. Applying eq 1 to the experimentally measured IV data permits values for R , G , n , and J_0 to be extracted for all samples listed in Table 1. The results of this analysis are presented in Table 2.

The resistance term, R , represents a "lumped" resistance associated with the bulk resistance associated with both the nanoporous and dense TiO₂ film layers, the measurement leads, and the TCO and graphite electrodes. For the 300nc samples, R is relatively constant (between 14 and 21 Ω cm²) for film thicknesses between 0 and 350 nm. The nanoporous film in these cases consists of isolated "clumps" or islands of TiO₂ nanoparticles dispersed on the dense TiO₂ substrate layer (this clumping is strongly indicated by Detak profilometer measurements of the thin 300nc films). The nanoporous layer "thickness", in this case, thus represents a mixing between the height of the nanoparticle clumps (~ 300 nm high) and zero thickness (where the dense layer is not covered by nanoparticles). In these films, because the film thickness is smaller than the particle size, conduction likely occurs through discontinuities in the nanoporous film. Series resistance in this domain is therefore controlled by the characteristics of the underlying dense TiO₂ layer. In the 300nc-1100nm sample, the nanoporous TiO₂ film thickness is greater than the particle size and additional series resistance is incurred due to interparticle hopping charge transport through the nanoporous film. R increases com-

mensurately. In the 9nc samples, R is even higher, and is dominated by the resistance of the nanoporous TiO₂ film. We have previously observed similar transport behavior trends in comparable nanoporous TiO₂ films.²⁸ There are several possible reasons for the significantly increased series resistance associated with the 9nc films: (1) increased resistance due to the significantly increased number of interparticle junctions, (2) increased resistance due to an increase in shallow traps, (3) increased resistance due to an increase in deep traps, and (4) increased resistance due to a decrease in donor density. The first two factors would effectively decrease the electron mobility, while the last two factors would decrease the effective carrier concentration. Trends in the other IV parameters, such as G , and J_0 , are not clearly resolved, although the diode ideality factor (n) increases substantially in the thickest films.

B. Dark MS Analysis. Representative MS curves for the samples discussed above are provided in Figure 1b. For all samples, the plateau capacitance (C_p) attained in the reverse bias (depletion) region is inversely proportional to the nanoporous TiO₂ film thickness. An effective medium model provides a good fit to the experimental data, indicating that the TiO₂ film behaves as a pure dielectric in the depletion region and that the internal surface area of the film does not contribute to the capacitance. (In other words, the electric potential drops uniformly across the nanoporous film.) Accounting for the measured porosity of the TiO₂ film and correcting for the dense TiO₂ underlayer, the effective dielectric capacitance may be calculated as

$$C_p^{-1} = \left(\frac{\epsilon_0 \epsilon_{\text{eff}}}{d_{\text{ncTiO}_2}}\right)^{-1} + \left(\frac{\epsilon_0 \epsilon_{\text{TiO}_2}}{d_{\text{DLTiO}_2}}\right)^{-1} \quad (2)$$

where the first term gives the capacitive contribution from the nanoporous TiO₂ layer (thickness d_{ncTiO_2}) and the second term gives the capacitive contribution from the dense TiO₂ underlayer (thickness d_{DLTiO_2}). In this equation, ϵ_0 is the permittivity of free space, ϵ_{eff} is the effective dielectric constant of the nanoporous TiO₂ film, and ϵ_{TiO_2} is the dielectric constant of the dense TiO₂ film. ϵ_{eff} accounts for the porosity of the nanoporous TiO₂ film through a statistical weighting function that takes into account the relative contributions from ϵ_{TiO_2} and ϵ_{air} based on the relative volume fractions of the two components. There are several effective medium theories that provide formulas for this statistical weighing function, including the Bruggeman theory,²⁹ the Maxwell–Garnett theory,³⁰ and the Landau–Lifshitz/Looyenga model^{31,32} (see ref 33 for an excellent discussion of the various effective medium theories). Although the Bruggeman theory is perhaps the most widely used, it is best applied in situations where the ratio of the dielectric constants for the two components is less than 20. Since air has a dielectric constant of 1 and TiO₂ has a dielectric constant of ~ 50 , application of the Bruggeman theory proves problematic (fluctuations in the local value of ϵ become unacceptably large). Likewise, it is difficult to use Maxwell–Garnett theory, which applies for binary systems in the limit where the volume fraction of one of the materials is small (less than 0.15). The porosity of our nanoporous films is between 56% and 66%, and therefore the volume fractions of both components are greater than 0.15. A third theory, the Landau–Lifshitz/Looyenga model, proves applicable to the nanoporous TiO₂ film. Furthermore, Theiss³⁴ has shown that the Landau–Lifshitz/Looyenga model is more topologically appropriate for porous materials than either the Bruggeman or Maxwell–Garnett models. For a two-component system consisting of air

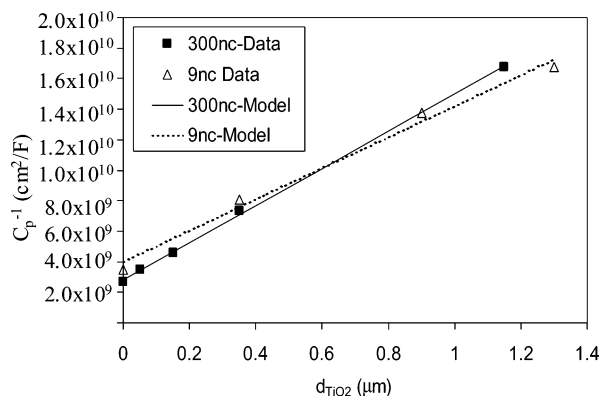


Figure 2. Inverse depletion capacitance (C_p^{-1}) versus nanoporous TiO_2 layer thickness for the 9nc and 300nc films. Depletion capacitance decreases with increasing nanoporous TiO_2 film thickness and can be fit to an effective medium capacitance model (linear fits).

and TiO_2 , the Landau–Lifshitz/Looyenga model yields

$$\epsilon_{\text{eff}} = [(\epsilon_{\text{TiO}_2}^{1/3} - \epsilon_{\text{air}})(1 - \phi) + \epsilon_{\text{air}}^{1/3}]^3 \quad (3)$$

where ϕ is the porosity (volume fraction of air), ϵ_{air} is the dielectric constant of air, $(1 - \phi)$ is the volume fraction of the nanocrystalline TiO_2 phase, and ϵ_{TiO_2} is the dielectric constant of bulk TiO_2 . (Lacking evidence otherwise, we assume that the bulk dielectric constant for TiO_2 is the same for the nanocrystalline and dense phases, although of course it must be modified by the porosity for the case of the nanoporous layer.)

By combining eqs 2 and 3, the experimental capacitance data for both the 9nc and 300nc films can be modeled. Figure 2 provides a comparison between the experimental data and model fit for both sets of films. For the 9nc crystallites, the best model fit is obtained with $\epsilon_{\text{TiO}_2} = 45$, while for the 300nc crystallites, the best model fit is obtained with $\epsilon_{\text{TiO}_2} = 65$. In both cases, ϵ_{air} is assumed equal to one. Both values fall within the range reported for nanocrystalline anatase TiO_2 and conform to the generally observed trend of decreasing dielectric constant with decreasing crystallite size.^{35–38}

As the data in Figure 2 reveal, the much larger internal surface area presented by the 9nc films compared to the 300nc films has no effect on C_p . The fact that C_p^{-1} is linearly dependent on film thickness but independent of particle size strongly justifies the effective medium interpretation.

Like the plateau capacitance, the apparent flat-band voltages extracted from the MS plots in Figure 1b also depend on film thickness. The apparent flat-band voltage increases with increasing nanoporous TiO_2 film thickness. This flat-band voltage offset effect can be modeled by assuming that the nanoporous TiO_2 film remains in the depleted (dielectric) state even at high voltages, so that band bending first occurs only in the dense TiO_2 layer. Thus, as the nanoporous TiO_2 film thickness increases, a correspondingly larger amount of voltage is dropped across this region. For band bending in a single n-type semiconductor layer, the Mott–Schottky equation expresses the linear relationship between C^{-2} and applied voltage (V):

$$C^{-2} = \frac{2}{\epsilon_0 \epsilon N_D} \left(V_{\text{fb}} - V - \frac{kT}{e} \right) \quad (4)$$

where e is the electron charge ($e = 1.6 \times 10^{-19}$ C), N_D is the donor density in the semiconductor (cm^{-3}), V is the applied voltage, and V_{fb} is the flat-band voltage. For a two-layer system, where ϵ and N_D may be different for each layer, the Mott–Schottky expression can be modified as³⁷

$$C^{-2} = \left(1 - \frac{\epsilon_1 N_{D1}}{\epsilon_2 N_{D2}} \right) \left(\frac{d_1}{\epsilon_0 \epsilon_1} \right)^2 + \frac{2}{\epsilon_0 \epsilon_2 e N_{D2}} (V_{\text{fb}} - V) \quad (5)$$

where subscripts 1 and 2 refer to the two layers of the system, respectively, and $N_{D1} < N_{D2}$. For the two-layer nanoporous TiO_2 + dense TiO_2 system, we assign ϵ_1 , N_{D1} , and d_1 to the nanoporous TiO_2 film and ϵ_2 and N_{D2} to the dense TiO_2 film. Again, it is necessary to account for the effect of porosity in the nanoporous region, therefore

$$\epsilon_1 = [(\epsilon_{\text{TiO}_2}^{1/3} - \epsilon_{\text{air}})(1 - \phi) + \epsilon_{\text{air}}^{1/3}]^3 \quad (6)$$

$$N_{D1} = (1 - \phi) N_{D,\text{ncTiO}_2} \quad (7)$$

where ϵ_1 is calculated by using the Landau–Lifshitz/Looyenga effective medium model, a simple linear rule-of-mixtures model is applied to estimate N_{D1} (simple porosity volume correction), and N_{D,ncTiO_2} represents the donor density in the TiO_2 particles.

For the nanoporous film to remain in depletion while band bending occurs in the dense film, the donor density in the nanoporous layer must be much lower than the donor density in the dense layer (in other words, $N_{D1} \ll N_{D2}$). This is reasonable, especially since the porosity of the nanoporous layer will certainly dilute the effective volumetric donor density (as per eq 7). Inserting the condition $N_{D1} \ll N_{D2}$ into eq 5 yields

$$C^{-2} = \left(\frac{d_1}{\epsilon_0 \epsilon_1} \right)^2 + \frac{2}{\epsilon_0 \epsilon_2 e N_{D2}} (V_{\text{fb}} - V) \quad (8)$$

The “apparent” flat-band voltage, V_o , is obtained when $C^{-2} = 0$. Setting eq 8 equal to zero, inserting V_o for V , and solving for V_o produces

$$V_o = \left(\frac{\epsilon_0 \epsilon_2 e N_{D2}}{2} \right) \left(\frac{d_1}{\epsilon_0 \epsilon_1} \right)^2 + V_{\text{fb}} \quad (9)$$

Thus, the apparent flat-band voltage (V_o) is offset from the real flat-band voltage (V_{fb}) by an amount that is proportional to the square of the nanoporous TiO_2 layer thickness (d_1^2). A quadratic fit to measured values of V_o versus nanoporous TiO_2 layer thickness permits extraction of the real flat-band voltage as well as the donor density in the dense TiO_2 layer, as shown in Figure 3. The fits shown in Figure 3 yield $V_{\text{fb}} = 1.7$ V and $N_{D2} = 2 \times 10^{15} \text{ cm}^{-3}$ for the 9nc TiO_2 samples and $V_{\text{fb}} = 1.65$ V and $N_{D2} = 1.65 \times 10^{15} \text{ cm}^{-3}$ for the 300nc TiO_2 samples. Reassuringly, the values are similar for the two samples, which should be expected since they share the same dense TiO_2 underlayer. The calculated donor density is considerably lower than typically observed in electrolyte-filled TiO_2 systems. In TiO_2 /electrolyte systems, N_D for spray-deposited TiO_2 is typically $10^{17}–10^{19} \text{ cm}^{-3}$.³⁹ The low donor density calculated here may reflect the fact that these tests, which are conducted in air, lead to increased oxygen vacancy passivation compared to electrolyte-filled TiO_2 experiments. The low donor density levels may also be a result of the prolonged air-annealing treatment at 450 °C employed after spray deposition.

The slope of the MS (C^{-2} vs V) plots in the space-charge region provides an independent measure of N_{D2} . From these slopes, (see Figure 1b) average values of $N_{D2} = 7 \times 10^{14}$ to $3 \times 10^{15} \text{ cm}^{-3}$ are obtained. Although this range brackets the values provided by the model fit, the donor densities calculated from the MS slopes appear to show a systematic increase with decreasing nanoporous TiO_2 layer thickness. The nature of this remarkable relationship has not been investigated any further.

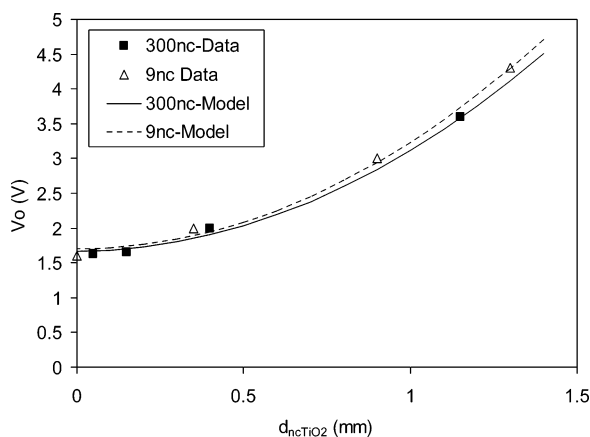


Figure 3. Apparent flat-band voltage (V_o) versus nanoporous TiO_2 layer thickness for the 9nc and 300nc films. The apparent flat band voltage increases quadratically with the nanoporous TiO_2 layer thickness. This behavior can be fit to a two-layer MS model assuming full depletion in the nanoporous TiO_2 film (model fits indicated).

One possibility is that our assumption of $N_{D1} \ll N_{D2}$ may be problematic. If N_{D1} and N_{D2} are similar, some mixture of band bending could occur. This may be particularly true for the thinner films, leading to systematic increase in the apparent MS slope with decreasing film thickness.

C. IV Analysis under Illumination. Under illumination, transport behavior changes significantly, as illustrated by the IV curves in Figure 4a. Under AM 1.5 illumination, the absolute magnitude of the current at a given voltage increases by almost a factor of 10 compared to the dark condition. This is a commonly observed effect in nanoporous TiO_2 films and is attributed to photodoping of the TiO_2 .^{17,18} Of the total AM 1.5 irradiation intensity of 1000 W/m^2 , approximately 5% is within the UV range. UV light with energy greater than the TiO_2 band gap (~ 3.2 eV) can be absorbed, leading to photogenerated charge carriers and thereby increasing the TiO_2 conductivity.

Also, the IV curves now show quasisymmetric rather than diode-like behavior. Diode analysis can no longer be used to interpret the transport behavior. Upon UV illumination the Fermi level splits in quasi-Fermi levels for electrons and holes. The presence of minority carriers (holes) changes the electrical contact with the graphite completely. Two nonblocking (ohmic) contacts are now present and current flow is limited by carrier transport rather than injection across a contact.

The hypothesis of carrier-transport limited current flow is supported by the J vs V^2 analysis of the IV data, as presented in Figure 4b. The linear dependence of J as a function of V^2 indicates that transport can be modeled by a space charge limited current (SCLC) process above a threshold voltage. Figure 5 recaptures the same IV data in log–log format to convey further details on the low-voltage IV dependence. For brevity, only the positive branches of the IV data are shown in Figures 4b and Figure 5; the negative branches show similar behavior.

The electron mobility in the nanoporous TiO_2 (μ_{ncTiO_2}) can be estimated from the SCLC region at high voltage. The standard SCLC model may be applied assuming that the SCLC limitation occurs only within the nanoporous TiO_2 layer, and neglecting the voltage loss across the dense TiO_2 layer:

$$J = \frac{9}{8} \epsilon_o \epsilon_{\text{eff}} \mu_{\text{eff}} \frac{V^2}{d_{\text{ncTiO}_2}^3} \quad (10)$$

where ϵ_{eff} is defined as per eq 3, $\mu_{\text{eff}} = (1 - \phi)\mu_{\text{ncTiO}_2}$, $V =$

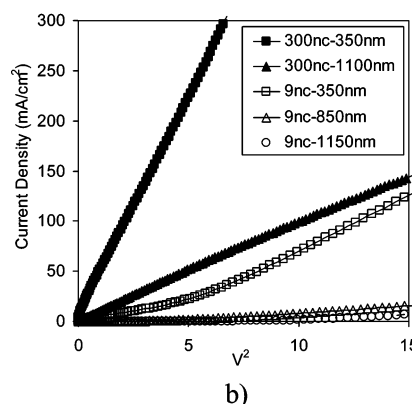
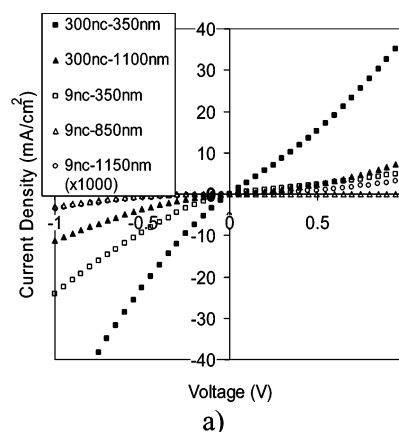


Figure 4. (a) IV curves and (b) the positive branch of the $I-V^2$ curves, for selected 9nc and 300nc films under AM 1.5 illumination. IV curves under illumination show nearly symmetric response. In a V^2 analysis, SCLC behavior is apparent at high voltages. Fits to a standard SCLC model permit extraction of electron mobility. The current–density values for the 9nc-1150nm IV curve have been amplified by a factor of 1000 for clarity.

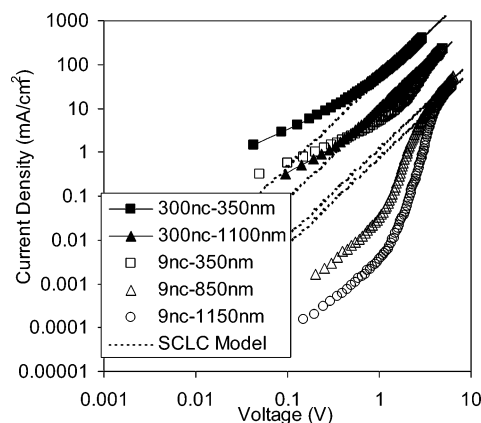


Figure 5. Log–log scale IV curves for selected 9nc and 300nc films under AM 1.5 illumination. The log–log analysis more clearly defines the onset voltage for the space charge limited current dependence. This onset voltage shifts to higher bias for thicker films.

applied voltage (volts), and all other terms are as previously defined. The resulting values of μ_{ncTiO_2} are summarized in Table 3.

The electron mobilities calculated from the SCLC model are roughly the same for both the 9nc and 300nc films and fall within the range reported in other recent experimental investigations.^{40,22}

Observation of Figure 5 reveals that the simple interpretation of ohmic (barrier-free) transport at low voltage transitioning to SCLC transport at high voltage is problematic for the thicker

TABLE 3: SCLC Model Electron Mobility Estimates under AM 1.5 Illumination from the IV Data in Figure 4b

sample	μ_{ncTiO_2} (cm ² /Vs)
300nc-350nm	3.5×10^{-4}
300nc-1100nm	1.8×10^{-4}
9nc-350nm	1.7×10^{-4}
9nc-850nm	2.3×10^{-4}
9nc-1150nm	3.4×10^{-4}

9nc-850nm and 9nc-1150nm films. In these films, most of the UV light is absorbed in the bulk of the TiO₂ nanoporous films, and very little UV light reaches the TiO₂/graphite interface. (Films are illuminated in a superstrate configuration, therefore the TiO₂/graphite interface is farthest from the incident light.) In these thicker films, therefore, the Schottky-barrier thermionic emission process is still believed to limit the IV response at low bias (as evidenced by the steep-slope rise to SCLC behavior).

IV. Conclusions

MS analysis indicates that the air-filled nanocrystalline TiO₂ films investigated in this contribution are fully depleted over a wide potential window in the dark. This behavior is captured by an effective medium model that averages the properties of the TiO₂ and air regions without taking into account structural features of the composite such as particle size or internal surface area. Depletion capacitance is observed to be insensitive to particle size (i.e., it does not depend on internal surface area), strongly justifying the effective medium interpretation. For thick films and small particle sizes, transport characteristics are increasingly dominated by a large series resistance contribution. This increased resistance could be attributed to trapping effects, to doping effects, or simply to an increase in interparticle-junction "bottlenecks" between TiO₂ particles. Dramatic differences in the dark-IV extrapolated resistance of comparable thickness 300nc and 9nc films indicate that the transport physics may be substantially different between these two types of films in the dark. Under illumination, conductivity improves substantially (this is attributed to photodoping) and the IV behavior is dominated by charge transport rather than charge injection. A space charge limited current model provides mobility estimates of $\sim(1.7\text{--}3.5) \times 10^{-4}$ cm² V⁻¹ s⁻¹ for both the 9 and 300 nm diameter TiO₂ particle films under illumination. The close agreement in illuminated-IV extrapolated electron mobility between the 9 and 300 nm diameter TiO₂ particles indicates that the transport physics are likely similar in both films when illuminated.

Acknowledgment. This material is based upon work supported by the National Science Foundation under Grant No. 0401817.

References and Notes

- O'Regan, B.; Grätzel, M. *Nature* **1991**, 353, 737.
- Bach, U.; Lupo, D.; Comte, P.; Moser, J. E.; Weissörtel, F.; Salbeck, J.; Spreitzer, H.; Grätzel, M. *Nature* **1998**, 395, 583.
- Hoffmann, M. R.; Martin, S. T.; Choi, D. W.; Bahnemann, D. W. *Chem. Rev.* **1995**, 65, 69.
- Fujishima, A.; Kohayakawa, K.; Honda, K. *J. Electrochem. Soc.* **1975**, 122, 1487.
- Bechinger, C.; Ferrere, S.; Zaban, A.; Sprague, J.; Gregg, B. A. *Nature* **1996**, 383, 608.
- Topoglidis, E.; Cass, A. E. G.; Gilardi, G.; Sadeghi, S.; Beaumont, N.; Durrant, J. R. *Anal. Chem.* **1998**, 70, 5111.
- Traversa, E. *Sens. Actuators, B* **1995**, 23 (2–3), 135.
- Eppler, A. M.; Ballard, I. M.; Nelson, J. *Phys. E* **2002**, 14, 197.
- Kelly, J. J.; Vanmaekelbergh, D. *Electrochim. Acta* **1998**, 43 (19–20), 2773.
- Zaban, A.; Meier, A.; Gregg, B. A. *J. Phys. Chem. B* **1997**, 101, 7985.
- Santiago, F. F.; Belmonte, G. G.; Bisquert, J.; Bogdanoff, P.; Zaban, A. *J. Electrochem. Soc.* **2003**, 150 (6), E293.
- Santiago, F. F.; Belmonte, G. G.; Bisquert, J.; Zaban, A.; Salvador, P. *J. Phys. Chem. B* **2002**, 106, 334.
- Ruhle, S.; Dittrich, T. *J. Phys. Chem. B* **2005**, 109, 9522.
- Greijer-Angrell, H.; Boschloo, G.; Hagfeldt, A. *J. Phys. Chem. B* **2004**, 108, 12388.
- Goossens, A.; Van der Zanden, B.; Schoonman, J. *J. Chem. Phys. Lett.* **2003**, 331, 1–6.
- Boschloo, G.; Hagfeldt, A. *J. Phys. Chem. B* **2005**, 109, 12093.
- Fabregat-Santiago, F.; Bisquert, J.; Garcia-Belmonte, G.; Boschloo, G.; Hagfeldt, A. *Sol. Energy Mater. Sol. Cells* **2005**, 87, 117.
- Wang, Q.; Moser, J. E.; Grätzel, M. *J. Phys. Chem. B* **2005**, 109, 14945.
- van de Lagemaat, J.; Park, N. G.; Frank, A. J. *J. Phys. Chem. B* **2000**, 104, 2044.
- Nelson, J.; Eppler, A. M.; Ballard, I. M. *J. Photochem. Photobiol. A* **2002**, 148, 25.
- Kytin, V. and Dittrich, T. H. *Phys. Status Solidi A* **2001**, 185 (2), 461.
- Konenkamp, R. *Phys. Rev. B* **2000**, 61 (16), 11057.
- Lin, H. M.; Keng, C. H.; Tung, C. Y. *Nanostruct. Mater.* **1997**, 9 (1–8), 747.
- Nanu, M.; Schoonman, J.; Goossens, A. *Adv. Mater. (Weinheim, Germany)* **2004**, 16 (5), 453.
- Nanu, M.; Schoonman, J.; Goossens, A. *Nano Lett.* **2005**, 5 (9), 1716.
- Snaith H. J.; Grätzel, M. *Adv. Mater.* **2006**, 18, 1910.
- Hegedus, S.; Shafarman W. N. *Prog. Photovoltaics* **2004**, 12, 155.
- O'Hayre, R.; Nanu, M.; Schoonman, J.; Goossens, A.; Wang, Q.; Gratzel, M. *Adv. Funct. Mater.* **2006**, 16, 1566.
- Bruggeman, D. A. G. *Ann. Phys. (Leipzig)* **1935**, 24, 636.
- Maxwell Garnett, J. C. *Philos. Trans. R. Soc. London, Ser. A* **1904**, 203, 385.
- Landau, L. D.; Lifshitz, E. M. In *Electrodynamics of Continuous Media*, 2nd ed.; Butterworth-Heinemann: Oxford, UK, 1984; p 42.
- Looyenga, H. *Physica (Amsterdam)* **1965**, 31, 401.
- Spanier, J. E.; Herman, I. P. *Phys. Rev. B* **2000**, 61 (15), 10437.
- Theiss, W. *Adv. Solid State Phys.* **1994**, 33, 149.
- Es-Souni, M.; Oja, I.; Krunks, M. *J. Mater. Sci.: Mater. Electron.* **2004**, 15 (6), 341.
- Garcia-Belmonte, G.; Kytin, V.; Dittrich, T. H.; et al. *J. Appl. Phys.* **2003**, 94 (8), 5261.
- Van der Krol, R.; Goossens, A.; Schoonman, J. *J. Electrochem. Soc.* **1997**, 144 (5), 1723.
- Mo, C. M.; Zhang, L. D.; Wang, G. Z. *Nanostruct. Mater.* **1995**, 6 (5–8), 823.
- Cameron, P. J.; Peter, L. M. *J. Phys. Chem. B* **2003**, 107 (51), 14394.
- Kytin, V.; Dittrich, T. H.; Bisquert, J.; Lebedev, E. A.; Koch, F. *Phys. Rev. B* **2003**, 68, 195308.